



## Research article

# Adaptive mesh refinement (AMR) criteria comparison for the DrivAer model



Oscar Irigaray<sup>a</sup>, Zugatz Ansa<sup>a</sup>, Unai Fernandez-Gamiz<sup>a,\*</sup>, Ander Larrinaga<sup>a</sup>, Roberto García-Fernandez<sup>a,b</sup>, Koldo Portal-Porras<sup>a</sup>

<sup>a</sup> Nuclear Engineering and Fluid Mechanics Department, University of the Basque Country, UPV/EHU, Nieves Cano 12, Vitoria-Gasteiz, 01006, Araba, Spain

<sup>b</sup> Sunsundegui S.A., Polígono Ibarrea, s/n, 31800, Altsasu, Navarra, Spain

## ARTICLE INFO

**Keywords:**

Adaptive mesh refinement  
DrivAer  
CFD  
Computational fluid dynamics

## ABSTRACT

Aerodynamics is one of the main areas of development in vehicle design. One of the most efficient ways of testing the aerodynamic design of a vehicle is to use Computational Fluid Dynamics (CFD), which allows for faster and more accurate aerodynamic simulations, which in turn helps increase the fuel economy and electric vehicle's range. Resource optimization is one of the most important aspects of CFD, and one of its main aspects is the spatial discretization of the fluid domain. This study discusses the use of Adaptive Mesh Refinement (AMR) for the aerodynamic design of private vehicles. This paper compares the results obtained with the use of AMR based on different fluid dynamic criteria for the DrivAer model and correlates the results with experimental data and computational results provided by various authors in previous publications. Four different optimization functions are defined and compared. The results for the drag coefficient, pressure coefficient, and total pressure wake have been correlated, showing great accuracy. This study has proven that the use of AMR highly optimizes computational resources by optimizing the mesh in the desired areas, thereby reducing the number of cells needed elsewhere. The use of these criteria has proven useful for drag coefficient prediction simulations because these criteria make use of the AMR to optimize the wake region.

## 1. Introduction

Owing to the latest developments in computational fluid dynamics and the increase in the importance of milage and energy efficiency (especially since the rise of electric vehicles), aerodynamics has become one of the most important branches of vehicle design. The latest developments in aerodynamics have produced several models to accurately represent and analyse the phenomena surrounding private vehicles passing through a mass of air. The main way to analyse and control wind energy by optimizing vehicle geometry has been Computational Fluid Dynamics (CFD). These recently optimized methods allow us to accurately predict the flow fields and aerodynamic loads around complex geometries. The world of aerodynamics engineering has been constantly improving the CFD methodology; therefore, the accuracy and efficiency of simulations have been growing exponentially.

One of the most widespread vehicle models used in the field of private transport is the DrivAer model. This model was developed by

\* Corresponding author.

E-mail addresses: [oirigaray001@ikasle.ehu.eus](mailto:oirigaray001@ikasle.ehu.eus) (O. Irigaray), [zansa001@ikasle.ehu.eus](mailto:zansa001@ikasle.ehu.eus) (Z. Ansa), [unai.fernandez@ehu.eus](mailto:unai.fernandez@ehu.eus) (U. Fernandez-Gamiz), [alarrinaga032@ikasle.ehu.eus](mailto:alarrinaga032@ikasle.ehu.eus) (A. Larrinaga), [rgarcia@sunsundegui.com](mailto:rgarcia@sunsundegui.com) (R. García-Fernandez), [koldo.portal@ehu.eus](mailto:koldo.portal@ehu.eus) (K. Portal-Porras).

<https://doi.org/10.1016/j.heliyon.2024.e31966>

Received 9 January 2024; Received in revised form 31 March 2024; Accepted 24 May 2024

Available online 24 May 2024

2405-8440/© 2024 The Authors. Published by Elsevier Ltd. This is an open access article under the CC BY-NC-ND license (<http://creativecommons.org/licenses/by-nc-nd/4.0/>).

the Technical University of Munich (TUM) as a joint project, together with Audi and the BMW Group [1,2]. The aim of this model is to provide a generic geometry that has the main characteristics of modern private vehicles and provide variations of this model to more accurately understand and predict flow fields around a wide range of private vehicle variants. Before 2012, less realistic private car models were available for manufacturers to test and understand the aerodynamic performance of their vehicles, especially in the wake area. Models such as the Ahmed body developed and studied by Ahmed [3,4] or SAE bodies parametrically studied by Cogotti [5].

The DrivAer model has been thoroughly tested using Wind Tunnel facilities and road tests by several different investigators and institutions, such as Cho et al. [6], who used the DrivAer model to test several drag reduction devices on passenger cars, specifically on the rear end of the vehicle. Ballerstein and Horst [7] and Nabutola and Boetcher [8] used CFD-based methods to develop and assess jet-wheel deflectors on passenger cars. The DrivAer model is freely distributed online by the Technical University of Munich (TUM) [9]. Other researchers also used the DrivAer model for their studies; for example, in 2018, Avadiar et al. [10,11] experimentally investigated the time-averaged wake through wind tunnel tests using velocity maps, drag force measurements, and base pressure distributions to characterize and quantify the flow behind and around the vehicle. They concluded that the up-wash caused by the flow exiting the smooth underbody diffuser dominated the near-wake and base-pressure distributions. In 2016 Christopher Collin et al. [12] carried out an investigation in which they performed a CFD simulation of the DrivAer model, precisely an unsteady Delayed Detached Eddy Simulation (DDES), to evaluate wind tunnel interferences for open jet test sections. Furthermore, experimental measurements of the 40 % scaled wind tunnel DrivAer model confirmed the relevance of wind tunnel effects for different blockage ratios and test section characteristics. In 2015, Miao et al. [13] introduced a new wind tunnel setup for the DrivAer model, a new suspension system that allowed the measurement of drag and lift forces while the wheels were rolling on the moving ground. They later compared the obtained data with numerical investigations, favourably concluding the correlation. Authors like the aforementioned Collin [12] or other authors such as James et al. [14] used Wind Tunnel testing and numerical computations to analyse the flow over the DrivAer model, creating therefore, a vast amount of both experimental and computational data which makes model validation more achievable when working on the DrivAer model. This is uncommon in the field of aerodynamics because of the scarcity of experimental data for contrasting purposes.

One of the main development areas of CFD is computational resource optimization and the overall efficiency of simulations. Owing to the high computational cost of obtaining accurate CFD representations, it is indispensable to optimize the available resources in the main areas of interest of the simulation. Optimizing the spatial discretization of the analysed domain is one of the most effective ways to optimize resources. By determining the areas of interest where the mesh density should be higher, we can reduce the number of cells needed elsewhere, thereby greatly enhancing the computational efficiency of our simulation. It is common to estimate the areas of interest based on theoretical knowledge of aerodynamic flow fields and previous experience. Although this method is also effective, the latest advances in computational science allow us to produce more accurate discretization of the areas of interest using output-based mesh optimization, also known as Adaptive Mesh Refinement (AMR). This method of mesh adaptation uses precomputed calculations to automatically determine refinement areas based on previous results for as many iterations as desired. This becomes an iterative process in which the variable of choice is analysed in each cell to determine whether the mesh should be refined or coarsened in that specific cell.

The use of AMR for CFD applications can vary significantly depending on the goal of the mesh refinement as well as the optimization parameters used. Different studies have used AMR to improve their simulation efficiency, such as Le Moigne [15], who studied unsteady delta-wing aerodynamics using AMR, and Lee and Kwon [16], who used AMR to refine the local vorticity maximum areas for multi-point aerodynamic optimization of rotor blades. Yang et al. [17] investigated the use of AMR combined with high-order (4th order) discretization schemes to solve highly vortical incompressible flows and a highly compressible shock-flow case.

Considering that AMR is an iterative process, the accuracy of the results depends heavily on the initial mesh, which must be fine enough to capture the phenomena occurring in the flow field, but coarse enough so that the refinement does not result in an over-production of cells.

The main aim of this study is to compare the results of AMR optimized simulations of the DrivAer model based on four different fluid dynamic criteria and to correlate the results with the available experimental and numerical data.

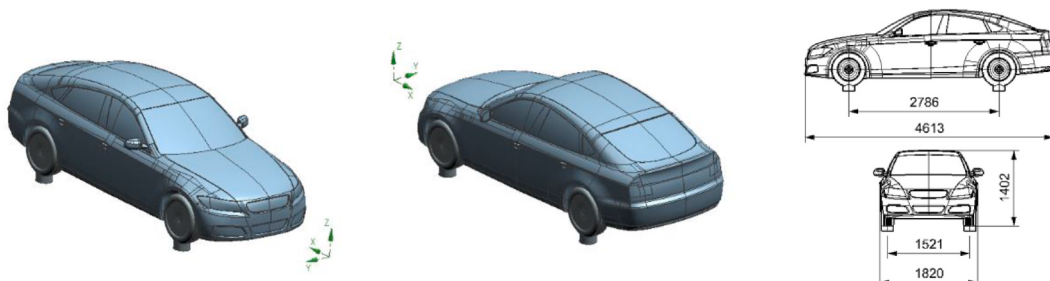


**Fig. 1.** DrivAer Fastback model.

## 2. Methodology

### 2.1. Geometry

For this study, as mentioned above, the analysed geometry consisted of the DrivAer model introduced by Heft et al. [1,2], specifically its fastback (FB) variant with a simplified smooth underbody, as shown in Fig. 1. This version of the DrivAer model has been chosen over other variants because it is the most used DrivAer model in CFD simulations owing to its simplified underbody geometry, which reduces the complexity of the mesh generation and its fastback-based rear-end shape, which is very common among passenger vehicle manufacturers. This geometry provides a wider set of experimental and computational data, which can be used to validate the development of our model.

To prepare the geometry for CFD purposes, some minimal alterations were included to ensure convergence of the simulation. One of the two main alterations was the elevation of the tires on the cylindrical structures to model the contact patch. This ensures that no acute angle is formed between the tire and road, which could result in a floating-point exception error. The second alteration of the geometry is the smoothing of the connection edge between the mirrors and bodywork. These edges were rounded and smoothed to allow for more accurate meshing and ensure a low wall  $Y+$  value to calculate the boundary layer in that area. These small modifications will introduce a small uncertainty, but they are expected to be orders of magnitude lower than the numerical errors and RANS errors.

### 2.2. Numerical set-up

#### 2.2.1. Boundary conditions

In terms of the boundary conditions for the simulations, every simulation was performed under a set of conditions defined to mimic and match the conditions defined by Heft et al. [2], as shown in Table 1. For the simulations, the 1:1 FB DrivAer model has been used and the double precision Star CCM + software were used [18]. Simulations were conducted for a constant density, time-averaged steady-state solution. The simulations were run for over 5000 iterations, and the convergence criteria were set at  $10^{-3}$  for all normalized residuals and a variance lower than 5 N for the drag force over at least 100 iterations. In addition, the drag force and drag coefficient ( $C_d$ ) values were averaged over the last 100 iterations. The simulation was run on an Intel Xeon Gold 5120CPU@2.2GHz with 28 cores and 56 threads and a RAM of 94 GB.

For the domain dimensions, a length of 20 L was defined to allow the development and dissipation of turbulent events in the wake of the vehicle. The width and height of the domain dimensions were 11 L and 15 L, respectively. These dimensions allow for a low blockage ratio ( $BR < 1\%$ ), which ensures that the walls do not have a significant effect on the flow field around the model according to Choi and Kwon [19], who studied the effect of BR on the aerodynamic behaviour of bluff bodies for a wide range of Reynolds numbers. Although this BR value can result in more realistic flow-field predictions, it is significantly lower than the experimental BR achieved in wind tunnel A of the Institute of Aerodynamics and Fluid Mechanics at the Technische Universität München, as shown by Heft et al. [1, 2].

The Reynolds conditions of the simulations were defined to ensure comparability of the results with both the experimental data and other CFD simulations performed by different authors, such as those performed by John. et al. [20], Peters et al. [21] and Collin et al. [12]. For this study, a Reynolds number of  $Re = 1.1 \times 10^7$  was used, as proven by Collin et al. [12], to be high enough to have sufficient  $C_d$  independence. This is equivalent to an inlet velocity of  $V = 140$  km/h for 1:1 DrivAer, which is a common testing speed.

Table 2 lists the model parameters used in the simulations. To mimic the conditions of the moving belt used in the experimental tests, a moving ground condition was defined using a sliding mesh, and a rotating motion was specified in all four tires, matching the speed of the inlet. The effect of rotating wheels on the flow field around the DrivAer model was studied by Aultman et al. [22]. Additionally, the effect of moving ground around the DrivAer model was studied by Wang et al. [23].

#### 2.2.2. Turbulence model

Private ground vehicles, such as those the DrivAer model tries to mimic, operate at relatively low Reynolds numbers, at which the flow field around them must be considered fully turbulent. This means that a turbulent model is required to resolve boundary-layer

**Table 1**  
Flow Domain dimensions in unit car length (L) and Boundary conditions.

Flow Domain Dimensions	
<i>Height</i>	11 L
<i>Length</i>	20 L
<i>Width</i>	15 L
<i>Blockage Ratio</i>	<1 %
Boundary Conditions	
<i>Ground</i>	No-slip and moving ground (140 km/h)
<i>Walls</i>	Slip
<i>Wheels</i>	Rotating wheels (123.46 rad/s)
<i>Inlet velocity</i>	38.89 m/s
<i>Half Car</i>	Symmetry plane

**Table 2**  
CFD model parameters and mesh configuration.

CFD model parameters	
Air density	1.184 kg/m <sup>3</sup>
Flow velocity	140 km/h
Turbulence model	K- $\omega$ SST
Convergence criteria	All residuals < 10 <sup>-3</sup> Variance of the drag < 5 N over 100 iterations
Mesh type	Trimmed Cell Mesher
Prism layers	20 layers, 15 mm thickness set for Y+ < 1
Number of cells (Base coarse mesh)	6 M Half car

(BL) interactions.

Reynolds Averaged Navier-Stokes (RANS) models have historically been the most used models in the field of ground vehicle aerodynamics. These models, although slightly less accurate than other physical and empirical models such as the Large-Eddy Simulation (LES) models owing to a slight loss of accuracy in the averaging process, can resolve the turbulence around the studied geometries with lower space discretization requirements, resulting in a reduced computational cost. Rüters et al. [24] simulated the DrivAer model using a 130 M cell (full car) using an LES model. Additionally, Rodi [25] proved that RANS models are more efficient than Direct Numerical Simulation (DNS) for relatively higher Reynolds values ( $Re > 10^4$ ) because of the high memory requirement increase in DNS with the Reynolds number. This requirement increase is due to the fact that the time step must be small enough that a fluid particle moves only a distance as big as the mesh spacing and additionally, every turbulence scale must be resolved, resulting in a higher density mesh requirement.

For this study, the k- $\omega$  (she stress transport SST (\*)) model developed by Menter [26], which comes from Wilcox's [27] original k- $\omega$  model, is used. This is one of the most used two-equation models because of its versatility and higher accuracy compared to other RANS models when resolving adverse pressure gradients. The k- $\omega$  SST model calculates the lower half of the BL using the original k- $\omega$  model, and instead, transitions to Jones-Launder's [28] k- $\epsilon$  model in the outer 50 % of the BL for higher Reynolds numbers and free shear layers. One advantage of this model with respect to other RANS models is that it accounts for shear stress transport in adverse pressure gradients, making it more accurate when predicting separation points and pressure recoveries.

Different studies, such as those carried out by Ashton and Revell [29], which compared different turbulent models for DrivAer geometry simulations, concluded that the model developed by Menter can produce accurate results with much less computational power requirements, such as those needed for Detached Eddy Simulations (DES) and Large Eddy Simulations (LES).

Menter's [26] k- $\omega$  SST model is defined by Equations (1)–(4).

$$\frac{\partial \rho \kappa}{\partial t} + \frac{\partial u_j \kappa}{\partial x_j} = P_k - \beta^* \rho \omega \kappa + \frac{\partial}{\partial x_j} \left[ (\mu + \sigma_\kappa \mu_t) \frac{\partial \kappa}{\partial x_j} \right] \quad (1)$$

$$\frac{\partial \rho \omega}{\partial t} + \frac{\partial u_j \omega}{\partial x_j} = \gamma P_\omega - \beta^* \rho \omega^2 + 2(1 - F_1) \sigma_{\omega 2} \frac{u_t}{\kappa} \frac{\partial \kappa}{\partial x_j} \frac{\partial \omega}{\partial x_j} + \frac{\partial}{\partial x_j} \left[ (\mu + \sigma_\omega \mu_t) \frac{\partial \omega}{\partial x_j} \right] \quad (2)$$

where:

$$P_k = u_t \frac{\partial u_i}{\partial x_j} \left( \frac{\partial u_i}{\partial x_j} + \frac{\partial u_j}{\partial x_i} \right) - \frac{2}{3} \rho \kappa \delta_{ij} \frac{\partial u_i}{\partial x_j} \quad (3)$$

$$P_\omega = \rho \frac{\partial u_i}{\partial x_j} \left( \frac{\partial u_i}{\partial x_j} + \frac{\partial u_j}{\partial x_i} \right) - \frac{2}{3} \rho \omega \delta_{ij} \frac{\partial u_i}{\partial x_j} \quad (4)$$

The set of constants  $\varphi$  is interpolated, Equation (5), from the constants  $\varphi_1$  and  $\varphi_2$  for k- $\omega$  SST and the k- $\epsilon$  models respectively as stated by Menter [26] using the following expression in which  $F_1$  varies from 1 to 0 as it gets away from the wall and closer to the boundary layer edge.

$$\varphi = F_1 \varphi_1 + (1 - F_1) \varphi_2 \quad (5)$$

Additionally, the eddy-viscosity is defined in Equation (6).

$$\nu_t = \frac{a_1 \kappa}{\max(a_1 \omega; \Omega F_2)} \quad (6)$$

where  $a_1 = 0.3$  and  $\Omega$  is the absolute vorticity value. Additionally,  $F_2$  is defined in Equation (7).

$$F_2 = \tanh \left( \max \left( 2 \frac{\sqrt{\kappa}}{0.09 \omega y}; \frac{400 \nu}{y^2 \omega} \right)^2 \right) \quad (7)$$

### 2.2.3. Spatial discretization (AMR)

For the spatial discretization of the domain, an initial hexahedral-based coarser mesh was defined (Fig. 2) such that all the governing phenomena occurring in the flow field were identified before the mesh optimization was carried out after the first convergence of the solution. Considering that the AMR is not configured to re-mesh the prism layers, they must be defined accurately for the coarser mesh. The prism layer configuration was set to obtain a nondimensionalized wall height value of  $Y+ < 1$  in every surface, so that the turbulence model resolves the wall instead of modelling it. Twenty layers were set over a thickness of 15 mm and a stretching factor of 1.5. The coarse mesh was composed of a total of 6 M cells. The mesh in the  $Y = 0$  m and  $X = 0$  m planes are shown in Fig. 2a and b respectively.

Once the initial mesh was developed, the simulation was run for approximately 500 iterations until convergence occurred. After initial convergence, the AMR is triggered, and the desired function is analysed at each cell and compared over a threshold. If the value of the cell is above or below this threshold, the hexahedral cells are divided or merged accordingly. In the first AMR iteration, the algorithm is not able to coarsen the original mesh; it can only refine it, but after that, the algorithm is able to coarsen a previously refined cell by merging it with the other refined mesh when the cell is below the lower threshold value. StarCCM+'s AMR algorithm refines the relevant domain volumes by splitting the hexahedral cells within the threshold values of any user specified function into eight cells by splitting the cell edges sides in half. This way the cell connectivity remains intact and the T-junctions at the boundaries between refinement levels are treated as any other manual volumetric refinement. As for the initialization of the solution on the newly split cells, the solution from the un-refined mesh is transferred to these cells (refined volumes will contain the same values as the final iteration on the coarser volumes from which they are formed).

**2.2.3.1. Laplacian of the total pressure.** For the first AMR optimization, the refinement criterion was defined based on previous knowledge of flows around ground vehicles, similar to the DrivAer model, with a special focus on accurately predicting the drag force and  $C_d$  of the model. Therefore, knowing the importance of the wake of the vehicle and how the geometry of the vehicle may affect it, the refinement criterion was based on the total pressure ( $P_T$ ). Because the wake of the vehicle is where the total pressure is lowest, the Laplacian of the  $P_T$  is appropriate. The Laplacian is defined as the divergence of the gradient of the scalar field. Therefore, this value will be greatest when the change in  $P_T$  increases as we move away from the cell we are evaluating; therefore, refining these areas will result in the refinement of the wake with more levels of refinement deeper into the close field wake, and it will fade out as it approaches the far-field and as we move outwards from the wake. To have an adapting field function that is updated after each refinement, said function must include the adaption cell size as a factor. This allows the user to control the minimum desired cell size and limit the refinement and cell count to the threshold values. Additionally, power factors must be included to prioritize and weigh the cell size over the refinement criteria. The refinement field function is defined in Equation (8).

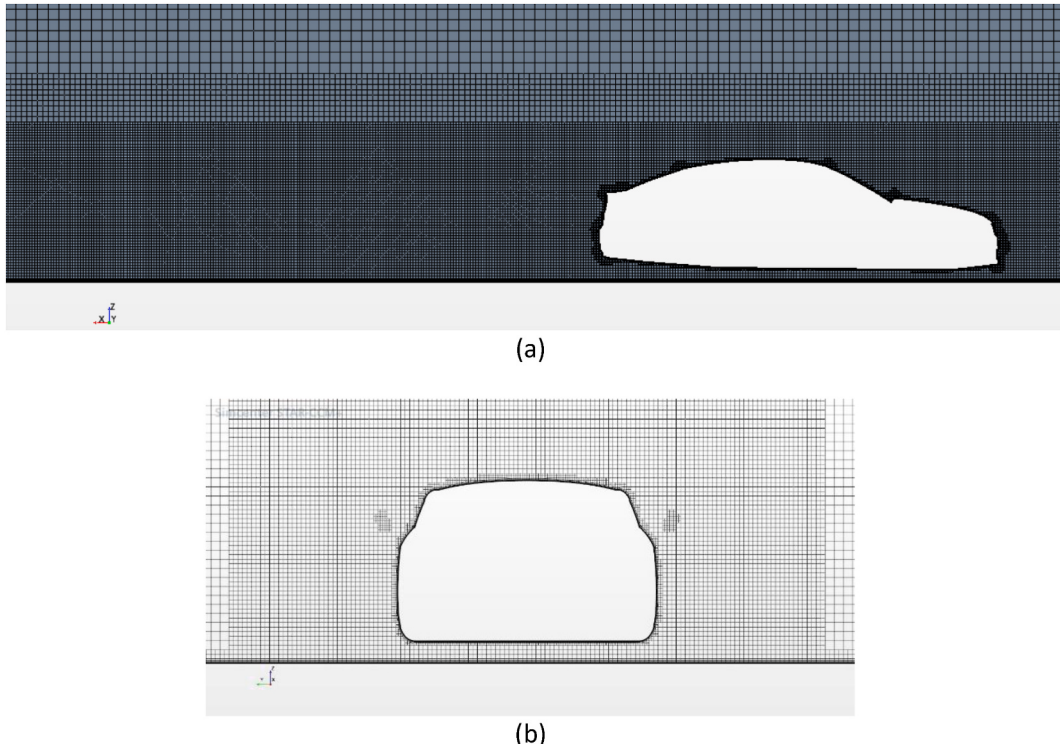


**Fig. 2.** Base mesh; (a)  $Y = 0$  m plane & (b)  $X = 0$  m plane.

$$(\nabla \bullet \nabla P_T) \bullet s_{Cell\ Size}^2 = \left( \frac{\partial^2 P_T}{\partial x^2} + \frac{\partial^2 P_T}{\partial y^2} + \frac{\partial^2 P_T}{\partial z^2} \right) \bullet s_{Cell\ Size}^2 \quad (8)$$

where  $P_T$  is the total pressure scalar field and  $s_{Cell\ Size}$  is the adaption cell size of each cell.

As for the threshold values, the upper limit was defined as 10, so that every cell over this value was refined and the lower value was set at 0.01, three orders of magnitude lower than the upper value, so that only the smallest cells were re-coarsened. AMR was run four times until all cells were below the upper limit, resulting in a final mesh of 73 M cells. The optimized mesh, Fig. 3a and c, and the refinement level of each cell are shown in Fig. 3b and d.

Further AMR optimization criteria were used to compare different mesh optimization methods with each other, as well as with experimental data. The goal of these new spatial discretization criteria is to focus on the wake region of a vehicle. This is because of the large importance of this region in the calculation of the drag force. Therefore, the goal will still be to calculate the drag force, but different approaches will be presented and compared.

**2.2.3.2. Turbulent Kinetic Energy.** The Turbulent Kinetic Energy (TKE) is defined by Pope [30] as the kinetic energy per unit mass of turbulent fluctuations. As the TKE is characterized by the RMS of the fluctuations of the velocity components associated with eddies in the flow, the TKE will be higher in regions such as the Boundary Layer and wake. Therefore, the TKE can be used as an optimizing criterion within the AMR solver. This results in a refinement of the wake region, as the boundary layer is already accounted for within the prism layer region of the mesh (which cannot be refined by the AMR solver). Equation (9) shows the second refinement method.

$$TKE \cdot s_{Cell\ Size} = \frac{1}{2} \left( \overline{(u')^2} + \overline{(v')^2} + \overline{(w')^2} \right) \cdot s_{Cell\ Size} \quad (9)$$

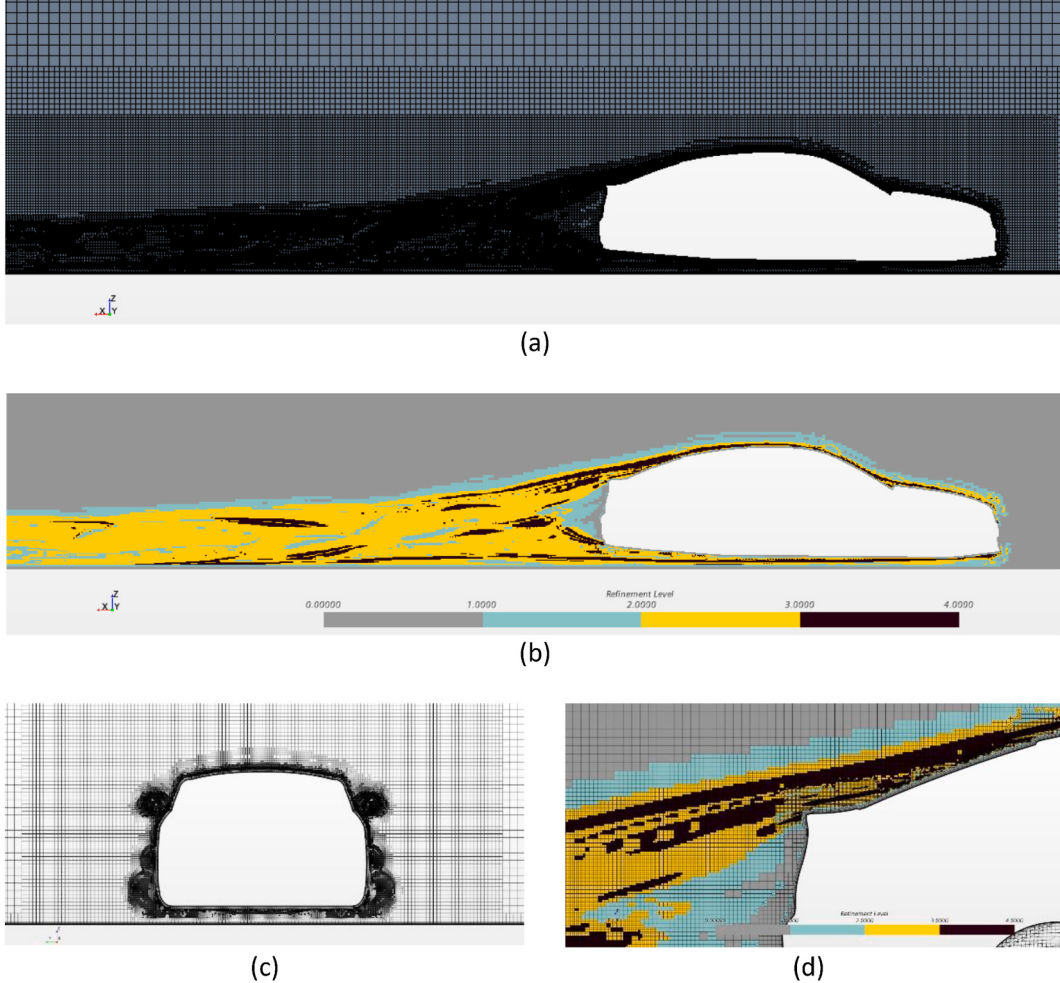


**Fig. 3.** Laplacian of the Total Pressure; (a)  $Y = 0$  plane mesh, (b)  $Y = 0$  refinement levels, (c)  $X = 0$  m plane mesh, (d) close-up of refinement levels with mesh at  $Y = 0$ .

where  $\overline{(u')^2}$ ,  $\overline{(v')^2}$  and  $\overline{(w')^2}$  are the variances of the velocity components (squares of the standard deviations) and  $s_{Cell\ Size}$  is the adaption cell size of each cell.

To define the refinement function, the TKE was multiplied by the adaption cell size to use the lower limit to stop the cell refinement. However, the cell size has not been squared to allow for better control of the final number of cells after refinement, as such factorizing would result in low values for the refinement function, making the final number of cells more sensitive to slight changes in the upper and lower limits. Said limits have been set at 0.25 for the upper limit and 0.001 for the lower one (2 orders of magnitude lower) to keep the resultant number of cells in de desired level ( $\sim 70M$ ). The resulting optimized mesh, Fig. 4a and c, and the refinement level of each cell are shown in Fig. 4b and d.

**2.2.3.3. Laplacian of the velocity magnitude field.** The third criterion that has been simulated and compared is the Laplacian of the Velocity magnitude. This case and the Total Pressure Laplacian have some similarities. The value was highest in the wake in both cases. This is because of the physical representation of the Laplacian means. The Laplacian is the divergence of the velocity-magnitude gradient vector field. Therefore, because the velocity magnitude is lowest at the bottom of the BL and wake, the gradient is greater at the outer edges of the wake, meaning that this will be the refinement area defined by the threshold. For the refinement function, the adaption cell size has been powered to a second grade to ensure that the cell size has a more limiting impact when defining which cells must be refined in each iteration, as well as obtaining the control function in the right range, Equation (10).

$$(\nabla \bullet \nabla \|U\|) \cdot s_{Cell\ Size}^2 = \left( \frac{\partial^2 \|U\|}{\partial x^2} + \frac{\partial^2 \|U\|}{\partial y^2} + \frac{\partial^2 \|U\|}{\partial z^2} \right) \cdot s_{Cell\ Size}^2 \quad (10)$$

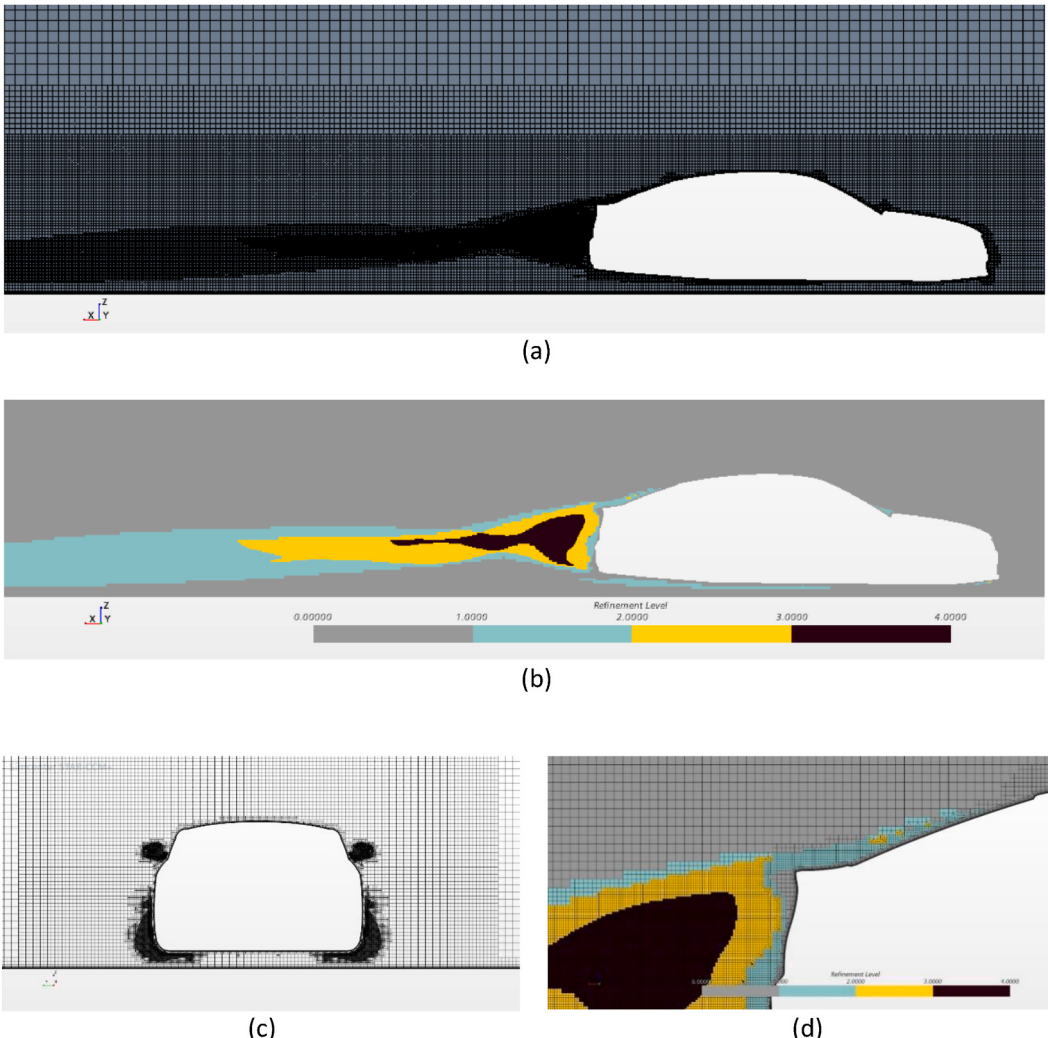


**Fig. 4.** Turbulent Kinetic Energy; (a)  $Y = 0$  plane mesh, (b)  $Y = 0$  refinement levels, (c)  $X = 0$  m plane mesh, (d) close-up of refinement levels with mesh at  $Y = 0$ .

where  $U$  is the velocity vector field, and  $\|U\|$  is the associated magnitude scalar field. Where  $s_{Cell\ Size}$  is the adaptation size of each cell.

The threshold was once again defined to control the maximum number of cells reached after the final refinement iterations to ensure that the simulation could be run with the available computational resources. The upper threshold value was set to 20, and the lower threshold value was set to 0.01. Fig. 5a and c shows the final mesh and Fig. 5b and d shows the number of refinement iterations for each cell.

**2.2.3.4. Root mean square of the curvatures of the velocity.** The last criterion that has been studied is the root mean square (RMS) of the curvatures of the velocity vector field in each Cartesian coordinate. In this case not only the wake of the vehicle will be refined but the whole “circulation” region. Wherever the velocity field was curved the most, the refinement was greater. Therefore, the wake will be refined the most once again, but in Fig. 6, we can see some additional refinement on the forward area of the vehicle, something that we could not see with the previous criteria.

For the control function, the selected criterion was multiplied by the adaption cell size squared to obtain the function in the desired range and to factor in the cell size as a control parameter, Equation (11).

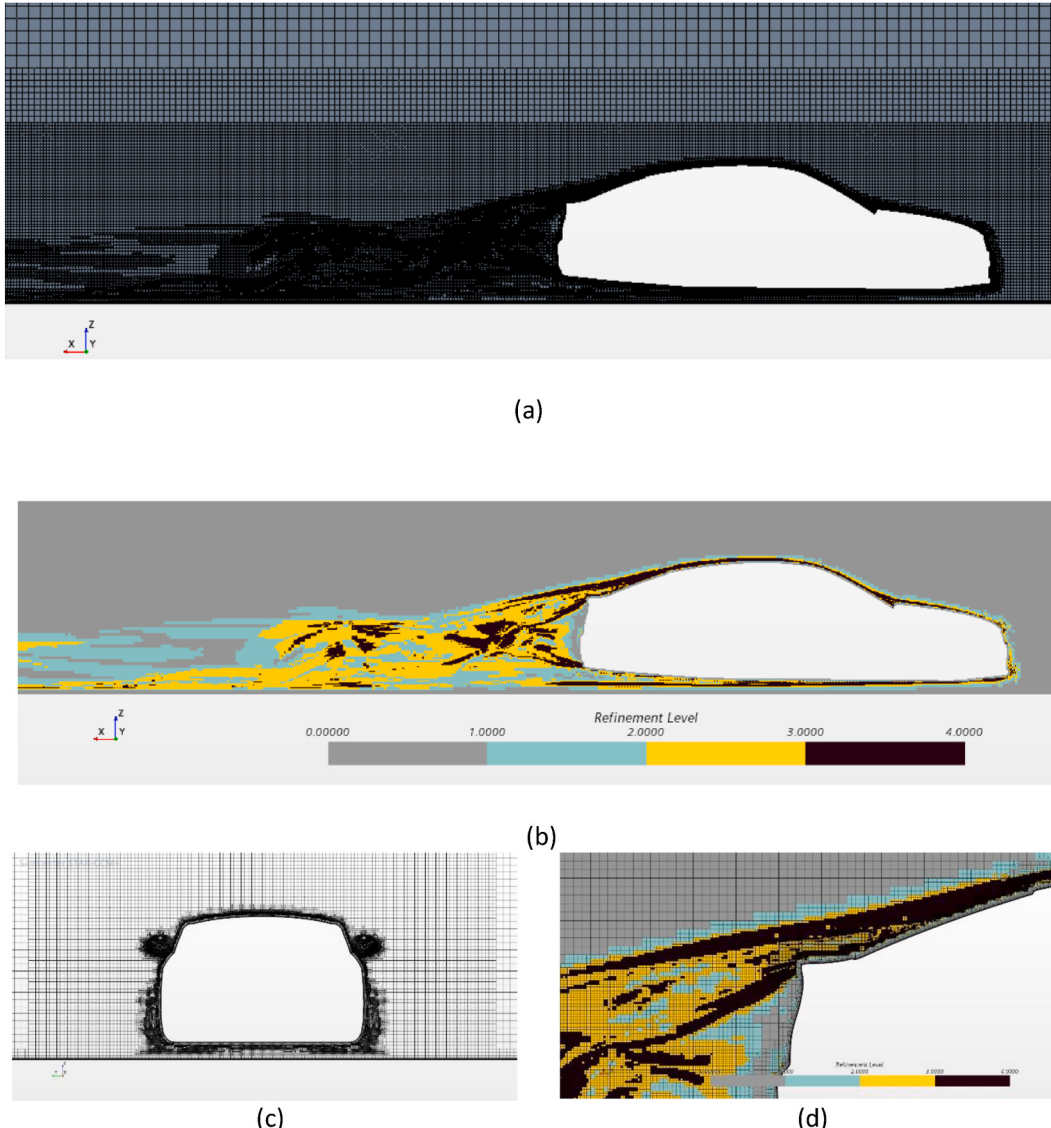


**Fig. 5.** Laplacian of the Velocity Magnitude; (a)  $Y = 0$  plane mesh, (b)  $Y = 0$  refinement levels, (c)  $X = 0$  m plane mesh, (d) close-up of refinement levels with mesh at  $Y = 0$ .

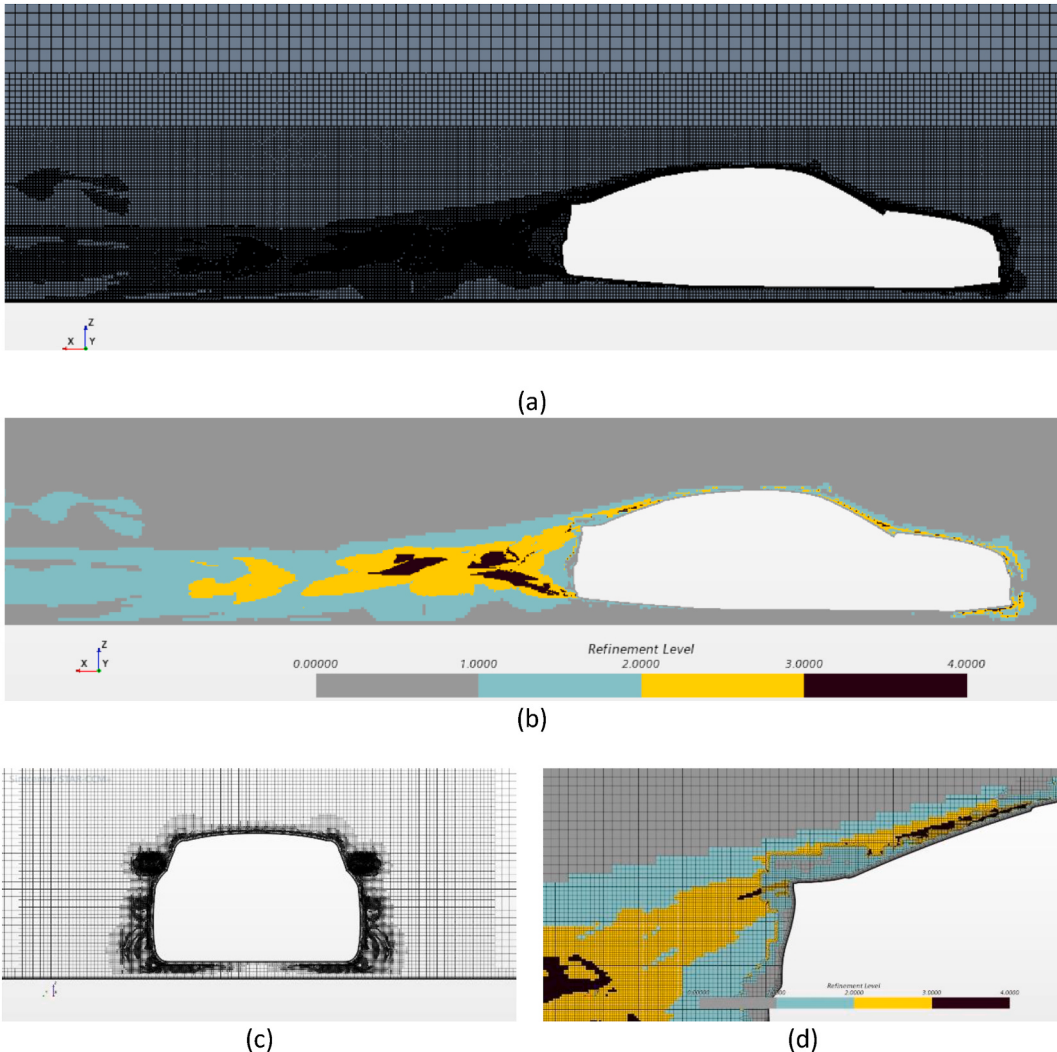


**Fig. 6.** RMS of Velocity Curvature; (a)  $Y = 0$  plane mesh, (b)  $Y = 0$  refinement levels, (c)  $X = 0$  m plane mesh, (d) close-up of refinement levels with mesh at  $Y = 0$ .

$$RMS_{Vel\ Curv} \cdot s_{Cell\ Size}^2 = \sqrt{\left(\frac{\partial^2 U}{\partial x^2}\right)^2 + \left(\frac{\partial^2 U}{\partial y^2}\right)^2 + \left(\frac{\partial^2 U}{\partial z^2}\right)^2} \cdot s_{Cell\ Size}^2 \quad (11)$$

where  $U$  is the velocity vector field, and  $s_{Cell\ Size}$  is the adaption cell size of each cell.

The threshold values were set at 0.5 for the upper value and 0.001 for the upper and lower values, respectively, resulting in the mesh shown in Fig. 6a and c. The refinement level of each cell are shown in Fig. 6b and d.

**2.2.3.5. Summary.** In summary, four AMR discretization criteria were defined, resulting in a total of five simulations (baseline included). The number of cells in each mesh and number of refinement iterations for each simulation are listed in Table 3.

**Table 3**  
Summary of AMR cases.

Simulation	Number of AMR iterations	Nr of Cells (Half Car)
Baseline	0	6 M
Total Pressure Laplacian	3	73 M
TKE	3	69 M
RMS Velocity Curvature	4	72 M
Velocity Magnitude Laplacian	3	75 M

Finally, Fig. 7 shows the mesh of the wake for the four different AMR criteria in the  $X = 4$  m plane. It can be observed that all four meshes are refined in the wake, as the main goal is to precisely predict the drag coefficient. Moreover, the meshes shown on the left-hand side are the Laplacian of the CpT in the top, Fig. 7a, and Laplacian of the V below, Fig. 7c, and it can be seen that both refinements are alike. The mesh on the top right-hand side shows the TKE refinement criterion, Fig. 7b, and the mesh below shows the RMS of the velocity curves, Fig. 7d.

### 3. Results

In the following section, the results of the carried work are analysed and compared with experimental data and results from other authors' work. The main results analysed are the drag coefficient ( $C_d$ ) value, surface pressure coefficient ( $C_p$ ) values over the top of the vehicle for a given middle plane, Total Pressure Coefficient ( $CpT$ ), or local energy of the fluid with respect to the initial energy in various planes of the wake region of the domain, and Q-criterion iso-surfaces with total pressure coefficient values for vortex visualization as the flow field is dominated by vortical structures and the separated wake. These are indispensable values when discussing the aerodynamic performance of a private vehicle as well as the efficiency of a CFD simulation.

#### 3.1. Drag coefficient

After performing the simulations, it is time to compare the results obtained. Table 4 compares the drag coefficient ( $C_d$ ) obtained in each simulation with experimental data from three different sources. The correlation between the computational and experimental values differs slightly for the coarser base mesh; however, as the mesh is refined, the  $C_d$  error is greatly reduced.

To compare the values, the Mean Absolute Percentage Error (MAPE), Equation (12), was used with respect to different experimental data values for the drag coefficient. The following formula was used:

$$MAPE(\%) = \frac{100\%}{n} \cdot \sum_{t=1}^n \left| \frac{E_t - v_{CFD}}{E_t} \right| \quad (12)$$

where  $n$  is the number of experimental data,  $E_t$  is the experimental drag coefficient value and  $v_{CFD}$  is the CFD obtained value.

From Table 4, it can be inferred that the Laplacian of the total pressure and TKE-based optimization methods provide the most accurate drag prediction results. In particular, the TKE-based mesh optimization provides not only accurate but also very precise results when compared with the three experimental values. However, every simulation shows a lower MAPE error for both the base 6 M cell simulation and lower error than the CFD simulation performed by Heft et al. [2]. This proves that the use of AMR optimizes the mesh resources for a better drag prediction capability. In this case, the selection criteria ensure that the desired mesh density is obtained in the wake area of the vehicle, whereas the cell density in the rest of the domain remains low.

#### 3.2. Pressure coefficient

In addition to  $C_d$  figures, it is essential to compare more experimental characteristics. Fig. 8 shows the pressure coefficient distribution on the central plane ( $Y = 0$  m) over the upper surface of the DrivAer model for both the study conducted by Heft et al. [2] and the AMR-based results. In the chart, the red line shows the experimental data obtained by Heft et al. [2], the green line shows the CFD

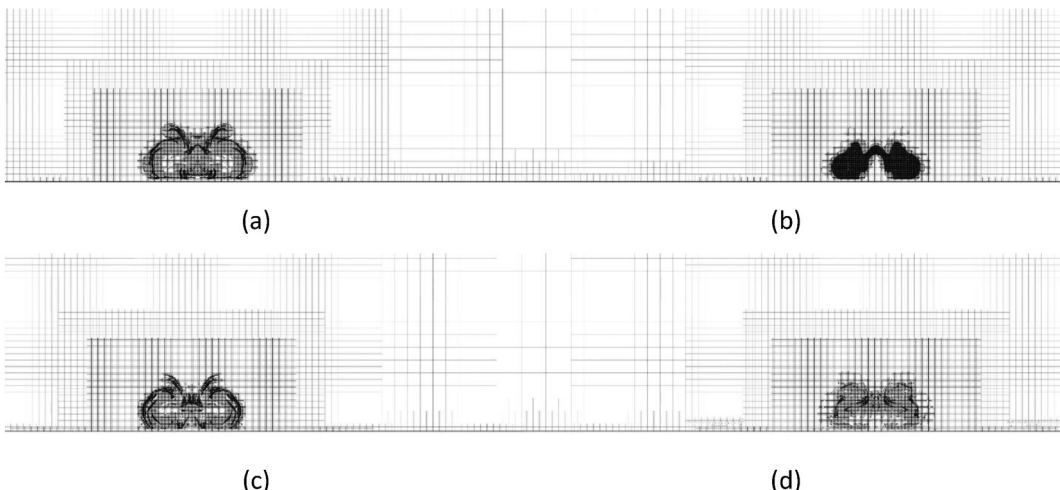


**Fig. 7.** Comparison of the refined meshes in plane  $X = 4$  m. (a) Laplacian of the Total Pressure, (b) Turbulent Kinetic Energy, (c) Laplacian of the Velocity Magnitude & (d) RMS Velocity Curvature.

**Table 4**  
Drag coefficient comparison.

Source	Cd	MAPE (%)
Experimental data Heft et al. [1]	0.254	-
Experimental data Collin et al. [12]	0.252	-
Experimental data Peters et al. [21]	0.256	-
CFD; Heft et al. [2] (19.4 M cells)	0.241	5.1 %
CFD; Base mesh (6 M cells)	0.262	3.0 %
CFD; AMR Lap Total Pressure (73 M cells)	0.253	0.7 %
CFD; AMR TKE (69 M cells)	0.254	0.5 %
CFD; AMR Lap V (75 M cells)	0.242	4.7 %
CFD; AMR RMS VCurv (72 M cells)	0.257	1.2 %

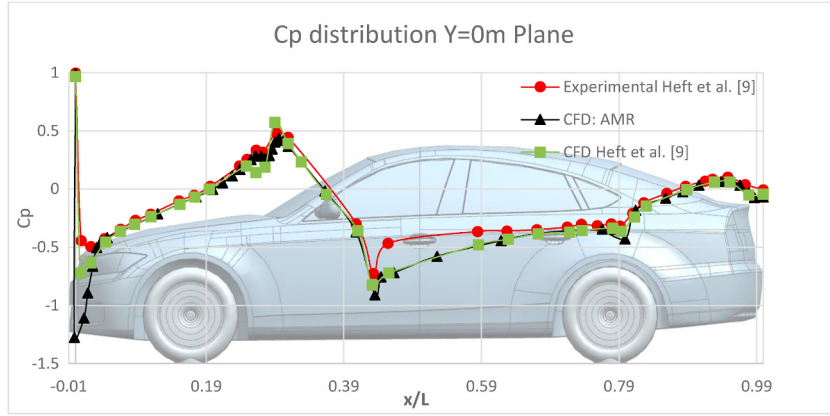


Fig. 8. Cp distribution chart on plane  $Y = 0$  m.

simulation of Heft et al. [2], and the dark line represents the CFD simulation performed by us. The stagnation point is clearly depicted in all three curves with the pressure peak. Subsequently, the flow accelerates as it flows over the hood, and the pressure drops abruptly. Then, the pressure constantly increased until the junction between the bonnet and the windshield. The pressure drops again as it accelerates over the windshield and then stabilizes over the top of the vehicle. The pressure was then recovered over the rear end of the FB model until it approached the atmospheric pressure in the near wake of the vehicle. All three curves showed a good correlation, with a few exceptions. The first pressure drop was overestimated by the AMR CFD simulation. However, the AMR simulation shows better correlation with the experimental data in the vicinity of the bonnet and windshield junction; however, it overpredicts the pressure drops at the top of the vehicle. Both CFD simulations show a strong correlation between them over the length of the top of the vehicle, but they slightly underpredict pressure recovery. This could be due to inefficient calculations of the adverse pressure gradient areas owing to errors in the turbulence model. Nevertheless, the overall agreement between the carried simulation and experimental data is good and demonstrates the efficiency of the AMR method. Moreover, the correlation between both CFD simulations depicted in Fig. 8

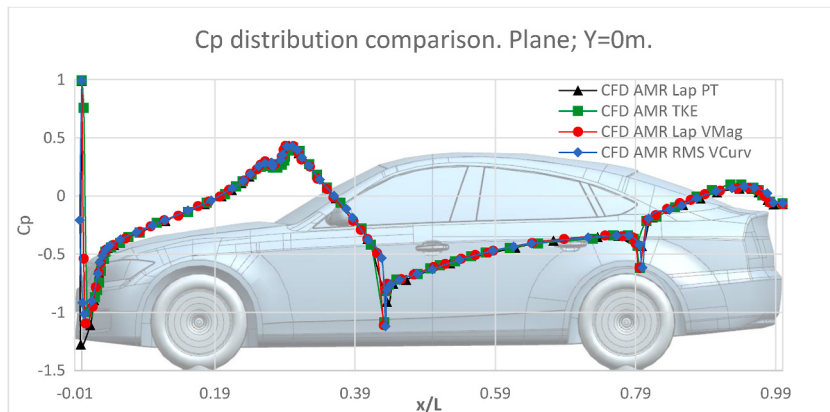


Fig. 9. Cp comparison for the different refinement criteria on plane  $Y = 0$  m

in terms of  $C_p$  is significant, with the only notable difference occurring in the first suction peak just downfield of the stagnation point.

Additionally, the comparison between  $C_p$  for the different AMR criteria is shown in Fig. 9, where the previously observed good correlation is confirmed for the rest of the criteria. It is worth mentioning that the correlation between the experimental data and all AMR CFD cases is particularly accurate in the rear region of the vehicle (over the rear window). This is obviously owing to the higher mesh density achieved after the AMR refinements.

As for the comparison of the pressure coefficients for the different criteria in Fig. 9, it can be seen that the TKE-based simulation does not overpredict the suction peaks as much as the other simulations. This is in accordance with the fact that this simulation produced the most accurate results for the drag coefficient prediction.

### 3.3. Total pressure coefficient in the wake region

Because the selected criteria for AMR focus on the wake of the vehicle, it is indispensable to analyse this area. Fig. 10 shows the prediction of the Total Pressure Coefficient ( $C_{pT}$ ) in the wake of the DrivAer model of the AMR-based CFD simulation in different sections along the fluid direction for the different refinement criterions; Fig. 10a shows the Baseline simulation, Fig. 10b shows the Laplacian of the total pressure, Fig. 10c shows the Laplacian of the velocity magnitude, Fig. 10d the TKE and Fig. 10e the RMS of the velocity curvatures.

Just behind the car, the energy is very low, as expected, but it approaches 1 (or free-stream  $C_{pT}$ ) as we move outward from the wake. As we move backward, the low-energy area dissipates across the field, and the wake becomes wider and lower. This suggests a downwash motion of the flow and gives us an idea of the light lift being produced. In addition, the wake shows two sets of rounded areas; the larger ones represent the merged inward rotating wake of the rear tires and the C-pillar vortices, and the smaller ones on the upper side of the wake represent the vortices generated by the mirrors.

Furthermore, Fig. 10 shows a comparison between the different wakes, as predicted by the different meshes. It is worth mentioning the differences between the different simulations are noteworthy. Fig. 10 (d) shows the low-energy wake predicted by the TKE-based optimized mesh. In this image, the different vortices are clearly distinguishable. Close to the ground and right behind the vehicle, the

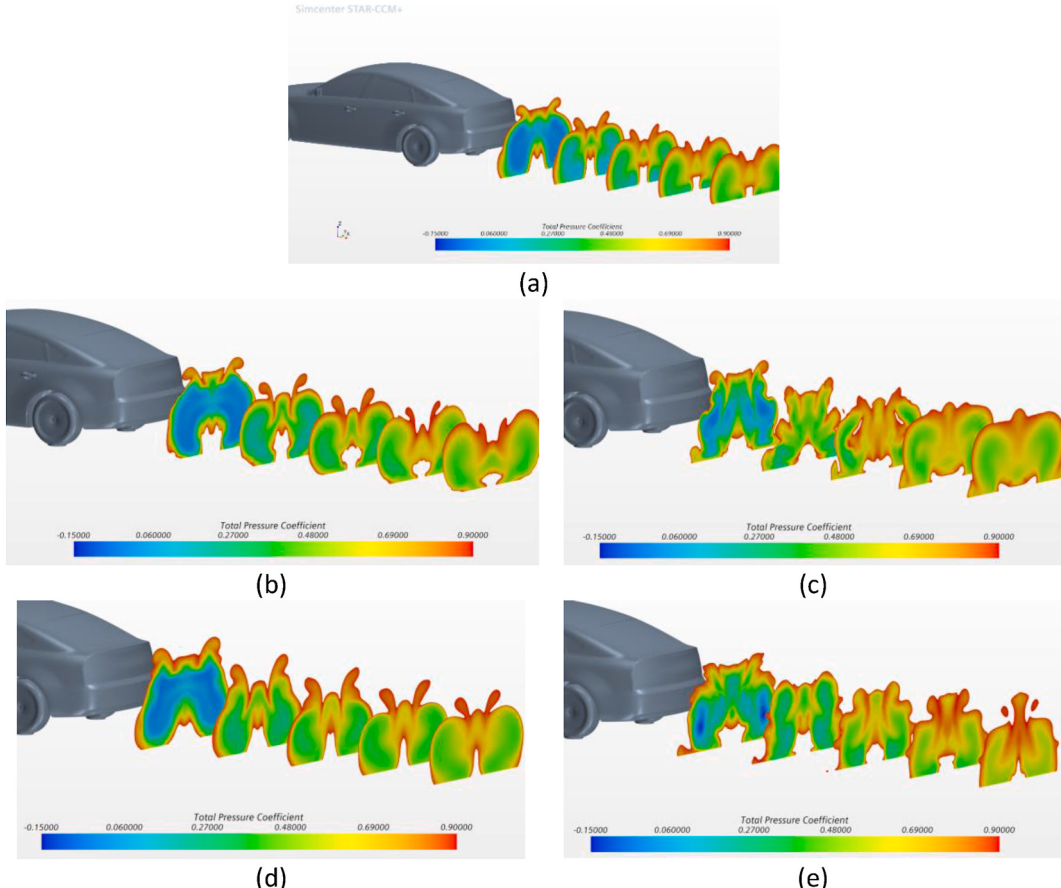


**Fig. 10.** Wake  $C_{pT}$  comparison in 5 different planes at  $X = 4$  m, 5.5 m, 7 m, 8.5 m and 10 m measured from the front axle. (a) Baseline, (b) Laplacian of the total pressure, (c) Laplacian of the velocity magnitude, (d) TKE and (e) RMS of the velocity curvatures.

rear tire vortices merged with those from the front tires. In addition, the development of the C-pillar vortex can be observed together with the rear-view mirror vortices. There is no available information to carry out a direct comparison on the specific planes showed with experimental data, however, it was thought that the comparison between the different simulations was interesting.

### 3.4. Q-criterion iso-surface

The Q-criterion is a very useful parameter in CFD because it is useful for visualizing vortical structures. In this case, a Q-criterion value of 1000/s was used to generate surfaces that visualized the main vortices in the flow field around DrivAer for the baseline and the four different AMR criteria. Fig. 11 shows the total pressure coefficient values for the iso-surfaces created using the Q criterion.

From Fig. 11, it can be seen how the differences in meshing affect the numerical dissipation and the difference in the vortices, as seen by the different meshes. Fig. 11a shows how the baseline simulation predicts the vortices. The mesh produced with the Laplacian of the total pressure, Fig. 11b, seems to have the least numerical dissipation as the “C-pillar” vortices depicted by the Q-criterion iso-surface on the upper part of the wake further reach the same vortices seen in the other three simulations, Fig. 11c (Laplacian of the velocity magnitude), Fig. 11d (TKE) and e (RMS of the velocity curvatures). However, it can be seen, that the higher-energy vortex shed from the rear-view mirrors reaches farther back in Figs. 11c and 11e than in the other two. This is due to the fact, that these two simulations use velocity as a base for refining instead of energy and since this vortex has a higher total pressure, its Laplacian value is not as high, resulting in a lower refinement of the vortex core and therefore some numerical dissipation.

Additionally, this Fig. 11 shows the evolution of the numerical diffusion with each of the remeshing algorithms, being the simulation based on the RMS of the velocity curvature, the one that shows the lowest numerical diffusion, based on the extent of the vortices displayed with the Q-criterion iso-surfaces.

### 3.5. Simulation time comparison

Finally, Table 5 shows the total CPU simulation time in both minutes and hours, required by each simulation to reach the defined convergence criteria. The simulation time in the AMR solvers, also includes the remeshing operation time for each time the AMR was triggered, thus significantly increasing the total simulation time.

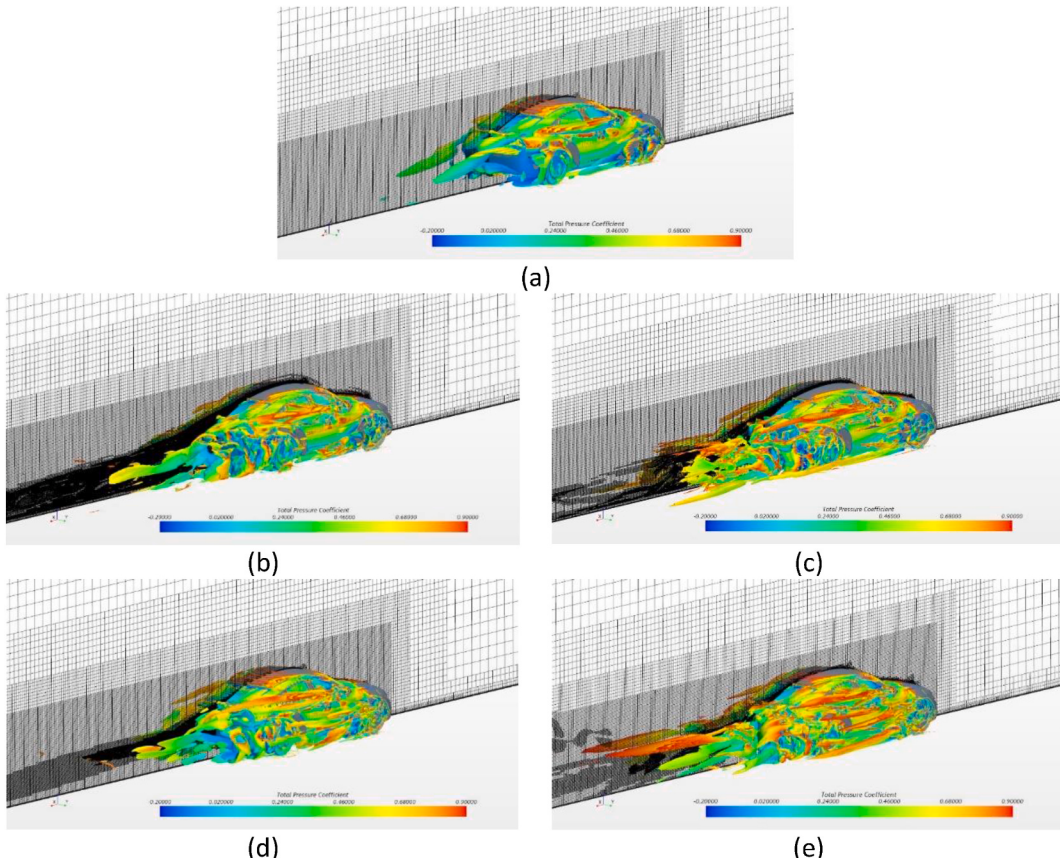


**Fig. 11.** Q-criterion iso-surfaces representing the CpT. (a) Baseline, (b) Laplacian of the total pressure, (c) Laplacian of the velocity magnitude, (d) TKE and (e) RMS of the velocity curvatures.

**Table 5**  
Simulation time comparison.

Case	Time [min]	Time [h]
Base mesh (6 M cells)	228.5	3.8
AMR Lap Total Pressure (73 M cells)	234.1	3.9
AMR TKE (69 M cells)	288.8	4.8
AMR Lap V (75 M cells)	650.5	10.8
AMR RMS VCurv (72 M cells)	673.5	11.2

Nevertheless, for the final number of cells in each of the cases, and thus for the final level of spatial resolution, the AMR simulations and specially the Turbulent Kinetic Energy based refinement, show a much more efficient behaviour considering that the final number of cells is more than ten times that of the baseline simulation. Thus, if the baseline simulation were to be refined to the point that the number of cells matched that of the AMR simulations, the result would yield a much longer simulation time, than those displayed by the AMR solvers, whilst producing larger errors, proving therefore its lower efficiency when compared to the use of AMR based simulations.

#### 4. Conclusions

In conclusion, this study developed a simulation for the DrivAer model in which an Adaptive Mesh Refinement method was implemented. Different criteria for refinement have been defined based on the experience of ground vehicle aerodynamics and the well-known importance of the wake. To do so, the refining criteria were coupled with the squared cell size to define four mesh refinement control functions.

In addition, the Adaptive Mesh Refinement (AMR) technique has been shown to be a powerful tool in Computational Fluid Dynamics (CFD) when applied to the DrivAer model. The DrivAer model is a popular test case for evaluating the aerodynamic performance of ground vehicles, and it can significantly improve the accuracy and efficiency of simulations.

The obtained results show a strong correlation with the experimental data and prove the effectiveness and efficiency of this method. This method can be used to optimize the effect of geometry alterations on the Cd of a vehicle, providing vehicle manufacturers with a great tool for vehicle design optimization and fuel consumption reduction. It has been demonstrated that AMR can significantly reduce the computational cost while maintaining the desired level of accuracy. By adaptively refining the mesh in the regions of interest, such as the wake behind the vehicle and coarsening it elsewhere, AMR can capture the important flow features and reduce the numerical diffusion and dissipation that are common in uniform grids.

Although this study only focuses on a specific geometry (the DrivAer model), the implementation of the AMR on CFD simulations can be extrapolated and integrated in other applications such as heavy vehicles and aviation, in order to carry out reliable and accurate simulations while maintaining the computational resources and simulation time under control.

Overall, this study demonstrates the potential of AMR to improve the accuracy and efficiency of the CFD simulations of the DrivAer model. Further research is required to fully understand the benefits and limitations of AMR in this application and to develop more advanced algorithms that can handle the complex flow physics and geometries encountered in realistic vehicle aerodynamics.

As for the comparison of the different refinement criteria defined in this study, the Turbulent Kinetic Energy (TKE) showed the most accurate results with the lowest number of cells out of all the cases studied. Nevertheless, the obtained results have been correlated with experimental data, showing great agreement for all cases, especially the pressure coefficient (Cp) results. Moreover, all cases produced more accurate drag coefficient (Cd) predictions than the base simulation. Thus, it is the authors recommendation that the Turbulent Kinetic Energy based algorithm is preferred, especially in the ambit of automotive design, as it results in the lowest errors in drag prediction, as well as, displaying the most efficient behaviour out of all the compared algorithms in terms of simulation time. However, if local pressures are to be accurately estimated for a local redesign of aerodynamic components, the Mean Velocity Curvature based AMR might be the preferred solution, as it produces the most accurate pressure coefficient values out of the 4 compared criteria when compared with experimental data.

#### Funding

The authors are thankful to the government of the Basque Country for the financial support of the ELKARTEK21/10 KK-2021/00014 and ELKARTEK20/78 KK-2020/00114 research programs. U.F.-G. was supported by the Mobility Lab Foundation, a governmental organization of the Provincial Council of Araba and the local council of Vitoria-Gasteiz.

#### Data availability statement

All data generated in the current study are available upon reasonable request from the corresponding author.

#### CRediT authorship contribution statement

**Oscar Irigaray:** Writing – original draft, Software, Methodology, Investigation, Funding acquisition, Formal analysis, Data

curation, Conceptualization. **Zugatz Ansa:** Methodology, Investigation, Data curation, Conceptualization. **Unai Fernandez-Gamiz:** Writing – original draft, Validation, Supervision, Project administration, Formal analysis, Data curation, Conceptualization. **Ander Larrinaga:** Writing – review & editing, Writing – original draft, Visualization, Formal analysis, Data curation, Conceptualization. **Roberto García-Fernandez:** Writing – review & editing, Writing – original draft, Visualization, Validation, Supervision, Project administration. **Koldo Portal-Porras:** Writing – review & editing, Writing – original draft, Visualization, Validation, Data curation, Conceptualization.

### Declaration of competing interest

The authors declare that they have no known competing financial interests or personal relationships that could have appeared to influence the work reported in this paper.

### Acknowledgments

The authors are grateful for the support provided by the SGIker of the UPV/EHU.

### References

- [1] A.I. Heft, T. Indinger, N.A. Adams, Introduction of a New Realistic Generic Car Model for Aerodynamic Investigations, 2012, 2012-01-0168.
- [2] A.I. Heft, T. Indinger, N.A. Adams, Experimental and numerical investigation of the drivAer model, in: Proceedings of the Proceedings of the ASME 2012; ASME: Rio Grande, Puerto Rico, 2012, p. 11.
- [3] S.R. Ahmed, An experimental study of the wake structures of typical automobile shapes, *J. Wind Eng. Ind. Aerod.* 9 (1981) 49–62, [https://doi.org/10.1016/0167-6105\(81\)90077-5](https://doi.org/10.1016/0167-6105(81)90077-5).
- [4] S.R. Ahmed, G. Ramm, G. Faltin, Some salient features of the time -averaged ground vehicle wake, *SAE Trans.* 93 (1984) 473–503.
- [5] A. Cogotti, A parametric study on the ground effect of a simplified car model, *SAE Trans.* 107 (1998) 180–204.
- [6] J. Cho, J. Park, K. Yee, H.-L. Kim, Comparison of various drag reduction devices and their aerodynamic effects on the DrivAer model, *SAE Int. J. Passeng. Cars – Mech. Syst.* 11 (2018) 225–238.
- [7] N. Ballerstein, P. Horst, Manipulation of the aerodynamic behavior of the DrivAer model using dimple patterns, *J. Wind Eng. Ind. Aerod.* 233 (2023) 105216, <https://doi.org/10.1016/j.jweia.2022.105216>.
- [8] K.L. Nabutola, S.K.S. Boetcher, Assessment of conventional and air-jet wheel deflectors for drag reduction of the DrivAer model, *Adv. Aerodyn.* 3 (2021) 29, <https://doi.org/10.1186/s42774-021-00086-7>.
- [9] Technical university of Munich geometrie available online. <https://www.epc.ed.tum.de/aer/forschungsgruppen/automobilaerodynamik/drivAer/geometrie/> (accessed on 14 March 2023).
- [10] T. Avadiar, M.C. Thompson, J. Sheridan, D. Burton, Characterisation of the wake of the DrivAer estate vehicle, *J. Wind Eng. Ind. Aerod.* 177 (2018) 242–259, <https://doi.org/10.1016/j.jweia.2018.04.013>.
- [11] T. Avadiar, M.C. Thompson, J. Sheridan, D. Burton, The influence of reduced Reynolds number on the wake of the DrivAer estate vehicle, *J. Wind Eng. Ind. Aerod.* 188 (2019) 207–216, <https://doi.org/10.1016/j.jweia.2019.02.024>.
- [12] C. Collin, S. Mack, T. Indinger, J. Mueller, A numerical and experimental evaluation of open jet wind tunnel interferences using the DrivAer reference model, *SAE Int. J. Passeng. Cars – Mech. Syst.* 9 (2016) 657–679, <https://doi.org/10.4271/2016-01-1597>.
- [13] L. Miao, S. Mack, T. Indinger, Experimental and Numerical Investigation of Automotive Aerodynamics Using DrivAer Model, American Society of Mechanical Engineers Digital Collection, 2016.
- [14] T. James, L. Krueger, M. Lentzen, S. Woodiga, K. Chalupa, B. Hupertz, N. Lewington, Development and initial testing of a full-scale DrivAer generic realistic wind tunnel correlation and calibration model, *SAE Int. J. Passeng. Cars – Mech. Syst.* 11 (2018) 353–367, <https://doi.org/10.4271/2018-01-0731>.
- [15] Le Moigne Adaptive Mesh Refinement and Simulations of Unsteady Delta-Wing Aerodynamics, 2004.
- [16] Lee Multi-Point Aerodynamic Shape Optimization of Rotor Blades Using Unstructured Meshes, 2007.
- [17] H.Q. Yang, Z.J. Chen, A. Przekwas, J.G. Dudley, Adaptive mesh refinement with high-order scheme for an unstructured pressure-based solver, in: American Institute of Aeronautics and Astronautics, vol. 52, National Harbor, Maryland, 2014.
- [18] Simcenter STAR CCM+ 2020.3.1 (15.06.008-R8) Double Precision, 2020.
- [19] Choi Wind Tunnel Blockage Effects on Aerodynamic Behavior of a Bluff Body, 1998.
- [20] M. John, S.-D. Buga, I. Monti, T. Kuthada, F. Wittmeier, M. Gray, V. Laurent, Experimental and Numerical Study of the DrivAer Model Aerodynamics, 2018, 2018-01-0741.
- [21] B.C. Peters, M. Uddin, J. Bain, A. Curley, M. Henry, Simulating DrivAer with Structured Finite Difference Overset Grids, 2015, 2015-01-1536.
- [22] M. Aultman, R. Auza-Gutierrez, K. Disotell, L. Duan, Effects of wheel rotation on long-period wake dynamics of the DrivAer fastback model, *Fluids* 7 (2022) 19, <https://doi.org/10.3390/Fluids7010019>.
- [23] S. Wang, T. Avadiar, M.C. Thompson, D. Burton, Effect of moving ground on the aerodynamics of a generic automotive model: the DrivAer-estate, *J. Wind Eng. Ind. Aerod.* 195 (2019) 104000, <https://doi.org/10.1016/j.jweia.2019.104000>.
- [24] M. Rüttgers, J. Park, D. You, Large-eddy simulation of turbulent flow over the DrivAer fastback vehicle model, *J. Wind Eng. Ind. Aerod.* 186 (2019) 123–138, <https://doi.org/10.1016/j.jweia.2019.01.003>.
- [25] W. Rodi, Comparison of LES and RANS calculations of the flow around bluff bodies, Elsevier, *J. Wind Eng. Ind. Aerodyn.* (1997) 55–75.
- [26] F.R. Menter, Improved Two-Equation K- $\omega$  Turbulence Models for Aerodynamic Flows, vol. 38, NASA, 1992.
- [27] D.C. Wilcox, Reassessment of the scale-determining equation for advanced turbulence models, *AIAA J.* 26 (1998) 1299–1310.
- [28] W.P. Jones, B.E. Launder, The calculation of low-Reynolds-number-phenomena with a two-equation model of turbulence, *Int. J. Heat Mass Transfer* 16 (1973) 1119–1130.
- [29] N. Ashton, A. Revell, Comparison of RANS and DES Methods for the DrivAer Automotive Body., Detroit, MI, USA, 2015, p. 11.
- [30] S.B. Pope, Turbulent Flows, Cornell University, New York, 2000, 978-0-521-59886-6.